Nanoscaled Zinc-Pyrazolate MOFs as Drug Delivery Systems

Sara Rojas,[†] Francisco J. Carmona,[†] Carmen R. Maldonado,[†] Patricia Horcajada,[‡,*] Tania Hidalgo,[‡] Christian Serre,[‡] Jorge A. R. Navarro[†] and Elisa Barea[†,*]

[†]*Department of Inorganic Chemistry, University of Granada. Av. Fuentenueva S/N, 18071 Granada, Spain*

[‡]*Institut Lavoisier, CNRS UMR8180, Université de Versailles St-Quentin en Yvelines, 45 Avenue des Etats-Unis, 78035 Versailles Cedex, France*

KEYWORDS. Porous coordination polymers, ruthenium metallodrugs, pore functionalization, RAPTA-C, mitoxantrone, nanocarrier.

ABSTRACT. This work describes the synthesis at the nanoscale of the isoreticular metal-organic framework series **ZnBDP_X**, based on the assembly of Zn(II) metal ions and the functionalized organic spacers 1,4-bis(1*H*-pyrazol- 4-yl)-2-X-benzene (H_2BDP_X; X = H, NO_2, NH_2 and OH). The colloidal stability of these systems was evaluated under different relevant intravenous and oral simulated physiological conditions, showing that **ZnBDP_OH** nanoparticles exhibit a good structural and colloidal stability probably due to the formation of a protein corona on their surface that prevents their aggregation. Furthermore, two antitumor drugs (mitroxantrone and [Ru(p-cymene)Cl_2(pta)]; pta = 1,3,5-triaza-7-phospaadamantane, RAPTA-C)

were encapsulated within the pores of the **ZnBDP_X** series in order to investigate the effect of the framework functionalization on the incorporation/delivery of bioactive molecules. Thus, the loading capacity of both drugs within the **ZnBDP_X** series seems to directly depend on the surface area of the solids. Moreover, ligand functionalization significantly affects both the delivery kinetics and the total amount of released drug. In particular, **ZnBDP_OH** and **ZnBDP_NH$_2$** matrices show a slower rate of delivery and higher percentage of release than **ZnBDP_NO$_2$** and **ZnBDP_H** systems. Additionally, RAPTA-C delivery from the **ZnBDP_OH** is accompanied by a concomitant and progressive matrix degradation due to the higher polarity of the BPD_OH ligand, highlighting the impact of functionalization of metal-organic framework cavities over the kinetic of delivery.

1. INTRODUCTION

In recent years, there has been a growing interest in the design of new submicronic or nanometric materials as carriers of challenging therapeutic agents, with the aim to solve important drawbacks associated with solubility, bioavailability, immunocompatibility and/or toxicity.[1,2] In this regard, a large panel of nanomaterials have been studied as drug delivery systems and/or contrast agents.[3] Among them, Metal-Organic Frameworks (MOFs), at the nanometric scale (nanoMOFs), have emerged as promising materials for biomedical applications due to their exceptional porosity and highly tuneable structure and composition.[4,5,6] Noteworthy series of nanoMOFs have been recently reported, exhibiting a wide variety of topologies and compositions, high adsorption capacity, adequate biocompatibility, biodegradation, etc.[7,8] However, the physicochemical properties of nanoMOFs (size, surface chemistry and chemical, structural and colloidal stability) govern their interaction with the biological surroundings. For instance, depending on the media (*i.e*. administration route), aggregation processes or adsorption of specific biomolecules (proteins, enzymes, lipids, etc.) on the outer surface of these nanomaterials may strongly influence their biodistribution within the body and thus, their efficiency.[9,10] In addition, particle size may also affect the drug delivery kinetics.[11] Prior to their application, it is therefore essential to carefully analyze the physicochemical properties of these nanoMOFs under different physiological conditions depending on the target administration route.[12,13] In this regard, few investigations have been recently reported dealing with the chemical and colloidal stability of nanoMOFs under physiological conditions.[14,15,16,17,18]

Among drug administration modes, parenteral and oral routes are the most commonly used in pharmaceutical applications. Parenteral route provides immediate onset of action but requires trained-staff and it is highly invasive, while non-invasive oral administration is low cost and

highly convenient for the patient, although exhibits some limitations such as hepatic first-pass metabolism or gastrointestinal degradation. Particle size, colloidal and chemical stability are critical parameters, which have to be adapted to the target administration route. For instance, intravenous route requires from nanoparticles smaller than 200 nm to prevent from embolic phenomena,[19] while smaller particles can increase the gastrointestinal residence time favouring the absorption of the carried drug.[20]

Among the most investigated nanoMOFs in the field of biomedicine so far, iron(III) polycarboxylate MOFs have been shown to be efficient for the controlled delivery of many important and challenging drugs. Although a controlled release in simulated body fluids was often achieved,[7b] one of the major drawbacks of these MOFs is their limited stability particularly at high pH (e.g. PBS, pH=7.2) leading in some cases to a rapid drug release.[21] It was shown previously that one way to increase the chemical stability of MOFs was to strengthen the metal-ligand bond using linkers such as imidazolates or pyrazolates,[22] affording in some cases exceptional chemical stabilities even under harsh conditions.[23,24] Thus, with the aim of increasing the chemical stability of the nanoMOFs, we optimized at the nanoscale the synthesis of zinc pyrazolate isoreticular series **ZnBDP_X** systems bearing complexing functions for intravenous and oral applications (< 200 nm). These materials, initially described by some of us,[25] are easily built from the assembling of Zn(II) cations and the previously functionalized bispyrazolate ligand (H_2BDP_X = 1,4-bis(1*H*- pyrazol-4-yl)-2-X-benzene, X = H, NO_2, NH_2 and OH; Figure 1). The tetragonal resulting materials (space group $P4_2/mmc$ (a = 13.2657 Å, c = 7.2474 Å, V = 1275.4 $Å^3$, Z = 2), present square channels with a free-pore aperture of 1.1 nm.[26] To our opinion, this **ZnBDP_X** family exhibits several advantages : (i) an *a priori* good biocompatibility as based on Zn^{2+}, an endogenous and essential cation to human life; (ii) their *a priori* high

biological stability, associated with the high basicity of the pyrazolate ligands and the hard-soft nature of the Zn^{2+}, which leads to the formation of robust Zn-N coordination bonds; and (iii) the possibility to easily functionalize the framework tuning their physicochemical properties; notably the interaction with biological structures or bioactive adsorbates, while reducing the risks of potential toxicity and/or accumulations effects.[27,28] In this line, it has been demonstrated that the pre-synthetic functionalization of the ligand H_2BDP by introducing $–NH_2$, $–NO_2$ and –OH groups in the isoreticular series **ZnBDP_X** led to a significant increase on the system affinity by the adsorption of polar gases.[25] Therefore, it is expected that a combination of factors such as the polarity, electron withdrawing or donating features and bulk of the substituents may influence the colloidal stability, porosity and uptake of the resulting metal organic framework nanoparticles.

On the other hand, it is well known that the use of Pt(II)-based cytotoxic metallodrugs, such as *cisplatin*, *cis*-[$Pt(NH_3)_2Cl_2$], and *carboplatin*, *cis*-[$Pt(CBDCA)(NH_3)_2$] (CBDCA: 1,2-cyclobutanedicarboxylato), are one of the most widespread treatments against cancer.[29,30] However, because of their associated adverse side effects and the development of resistance related to the unspecific interactions of Pt(II) metallodrugs with the desired biological target, it is necessary to develop new chemotherapeutic agents able to improve the effectiveness and specificity of the cancer treatment. In this sense, a new series of half-sandwich ruthenium compounds with an important antitumoral activity has recently emerged. The success of these new ruthenium metallodrugs lies in their ability to interact with different biological targets (*i.e.* inhibition of over-expressed enzymes, such as cathepsines)[31,32] and/or the inference with physiological redox processes,[33] leading to various and combined mechanisms of action. In particular, the non-conventional metallodrug [Ru(*p*-cymene)Cl_2(pta)] (pta = 1,3,5-triaza-7-

phospaadamantane) termed RAPTA-C (Figure 1), has demonstrated to inhibit lung metastases in mice.[34]

In addition, pure organic molecules are also widely used in cancer chemotherapy. In particular, anthracyclines with a cytotoxic activity essentially related to their non-covalent binding to DNA double helix.[35] Among this family, the anthraquinone derivative mitoxantrone (Figure 1), is one of the most promising compounds, having proved a relevant activity against advanced breast cancer, non-small cell lung cancer as well as non-Hodgkins lymphoma.[36,37,38]

Considering the above information and the fact that both drugs present several drawbacks related with their poor stability against the physiological media and their important toxicity related with their unspecific delivery,[84] we propose here the encapsulation and delivery of both anticancer drugs (RAPTA-C and mitoxantrone) into the porous structure of **ZnBDP_X** series in order to develop a more efficient treatment, protecting the drugs from degradation and delivering them in a controlled manner at the target site.

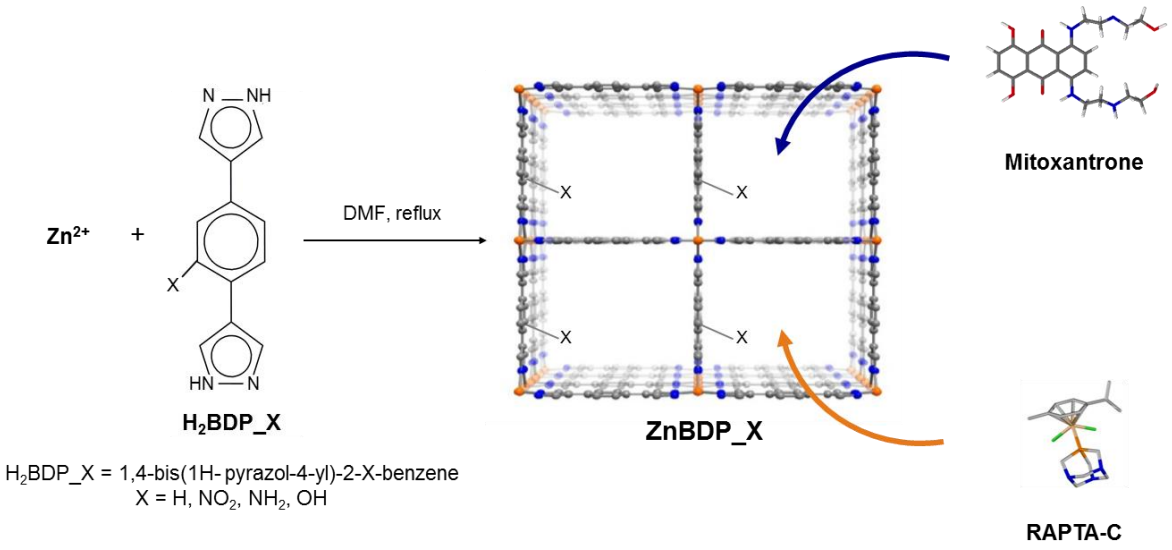

Figure 1. Schematic representation of the reaction between Zn(II) and the functionalized ligands H_2BDP_X to obtain the isoreticular **ZnBDP_X** series for the encapsulation of the non-conventional

anticancer drugs RAPTA-C and mitoxantrone. Zn, N and C atoms are in orange, blue and grey, respectively.

Thus, we have first synthesized a series of four isoreticular functionalized MOFs at the nanoscale [**ZnBDP_X**; X = H, NO_2, NH_2, OH] with a particle size compatible with the intravenous and oral administration routes. A particular attention has been paid to the kinetics of crystallization through a combination of X-ray powder diffraction (XRPD), dynamic light scattering (DLS), field emission gun scanning electron microscopy (FEG-SEM) and reaction yield estimation. Moreover, the structural and colloidal stability of these nanoMOFs has been investigated under simulated intestinal and serum conditions as a function of the MOF functionalization, in order to evaluate their possible use as oral or intravenous drug nanocarriers. Finally, the influence of the functional group of the synthesized ZnBDP_X nanoMOFs has been investigated on the loading and release kinetics profiles of two challenging antitumor drugs (RAPTA-C and mitroxantrone).

2. EXPERIMENTAL SECTION

2.1. Materials

All chemicals were commercially obtained and used without further purification. Zinc 2,4-pentanedionate monohydrate was purchased from Alfa Aesar (12527), mitoxantrone from Shangai IS Chemical Technology, and $RuCl_3$ from C. J. Chambers Hispania S. L. Zinc acetate hydrate (R252506), α-terpinene (> 95.0%, 86473), phosphate buffered saline (PBS) solution (P4417, pH = 7.4, 0.01 M), mucin from porcine stomach (M1778, partially purified), bovine serum albumin (BSA, A7030, lyophilized powder, 98%), pancreatin from porcine pancreas (P3292, powder) and solvents (*N,N'*-dimethylformamide (DMF), dimethyl sulfoxide (DMSO),

propan-2-ol, ethanol and methanol) were purchased from Sigma-Aldrich. RPMI 1640 medium was purchased from Gibco. The 1,4-bis(1H- pyrazol-4-yl)benzene ligand (H_2BDP) and the nitro-, amino- and hydroxo- derivatives (H_2BDP_X, X = NO_2, NH_2 and OH) were prepared as previously described in the literature.[25,39] [Ru(*p*-cymene)Cl_2(pta)] (pta = 1,3,5-triaza-7-phospaadamantane) was synthesized according to literature.[40]

2.2. Conventional synthesis of ZnBDP_X

H_2BDP_X (0.5 mmol) was dissolved in DMF (40 mL) in a 50 mL Schlenk-flask and heated up to 150 °C. $Zn(CH_3COO)_2 \cdot 2H_2O$ (0.5 mmol) was then added to the previous solution under stirring. The mixture was allowed to react for 7 h under reflux. After being cooled-down to RT, the solid was collected by centrifugation (10500 rpm / 10 min), washed with DMF (2 x 10 mL) and with ethanol (2 x 10 mL). The solids were dried at 200 ºC for 12 h under vacuum. Typical yields of the desolvated MOF were 55±5 %.

The evolution of the particle size of **ZnBDP_X** was monitored during the synthesis by collecting several aliquots (1.5 mL) at different reaction times (considering as starting time the addition of the Zn precursor). The collected aliquots were centrifuged (14000 rpm / 1 min.) and washed with DMF (3 x 1.5 mL). Particle size was estimated by different methods (Scherrer's equation from XRPD, SEM and DLS). DLS measurements were carried out by redispersing the sample in DMF (1 mg mL^{-1}) using an ultrasound tip (10% amplitude and 20 s; Digital Sonifer 450W). The remaining sample was filtered and XRPD and SEM characterizations were performed.

2.3. Green synthesis of **ZnBDP_OH**

Microwave synthesis was performed on a Mars 5 microwave system (1600 W, 2450 MHz; USA). H_2BDP_OH (0.04 mmol) and Zn^{2+} precursor ($Zn(AcO)_2$ or Zn(2,4-pentanedionate)$_2$; 0.04 mmol) were mixed in 1.5 mL of propan-2-ol using a 3.5 mL-volume reactor. The mixture was heated up to 100 ºC for one hour with a heating ramp of 3 minutes by microwave radiation using a power of 600 W. After being cooled-down to RT, the solid was collected by centrifugation (14000 rpm / 1 min), washed with DMF (3 x 10 mL) and dried under vacuum. The reaction yield for both Zn precursors was *ca*. 50%. DLS, SEM and XRPD characterizations were performed.

On the other hand, **ZnBDP_OH** was also obtained under conventional reflux conditions using propan-2-ol as solvent. In a typical synthesis, H_2BDP_OH (0.5 mmol) was dissolved in propan-2-ol (40 mL) in a 50 mL Schlenk-flask and heated at 80 °C. $Zn(CH_3COO)_2{\cdot}2H_2O$ (0.5 mmol) was then added to the previous solution under stirring. The mixture was allowed to react for 24 h under reflux. The hot solution was filtered and the solid was washed with propan-2-ol (2 x 10 mL).

2.4. Characterization

Prior to the analyses, 100 mg of sample were heated under vacuum (10^{-2} KPa) at 200 ºC overnight in order to remove the free solvent (ethanol, propan-2-ol, water, DMF) entrapped into the pores. Infrared spectroscopic (IR) analyses were performed in a Thermo Scientific Nicolet™ 6700 FTIR spectrometer. N_2 isotherms were obtained at 77 K using a Belsorp Mini (Bel, Japan) and a Micromeritics Tristar 3000 volumetric instrument. Routine XRPD patterns were collected using a high-throughput Bruker D8 Advance diffractometer working on transmission mode and equipped with a focusing Göbel mirror producing CuKα radiation (λ = 1.5418 Å) and a LYNXEYE detector. Data were collected at room temperature (RT), in the 2θ range 3 to 30˚,

with a 0.02˚ step width. For further XRPD studies (determination of particle size and Scherrer's equation calculations), XRPD patterns were collected in a conventional high-resolution D5000 Siemens X'Pert MDP diffractometer (θ - 2θ) using λ_{Cu}, $K_{\alpha1}$, $K_{\alpha2}$ radiation (λ = 1.54051, 1.54433 Å), from 5 to 30˚ (2θ), a step size of 0.02˚ and 22 s *per* step in continuous mode. Thermogravimetric analysis were performed using a Mettler Toledo TGA/DSC STAR system under oxygen flow (20 mL min^{-1}) running from RT to 600 °C with a heating rate of 2 °C min^{-1}. FEG-SEM was carried out using a JEOL JSM 6335F microscope at 15 kV coupled to Oxford Instruments X-Max 80 mm^2 unit. The crystal sizes (d_{XRD}) were calculated using XRPD obtained at different reaction times. d_{XRD} were estimated from the broadening of the 100 Bragg peak, using Scherrer's equation (eq. (1)):

$$d_{XRP} = \frac{K\lambda}{\beta \cos\theta} \qquad (1)$$

where θ is the Bragg angle of diffraction lines, K is a shape factor taken as 1, λ is the wavelength of incident X-rays (1.5406 Å), and β is the line broadening at half the maximum intensity (FWHM).[41] On the other hand, nanoparticle size distribution was studied by SEM images using "ImageJ'' software for image processing and analysis.[42] The mean particle size was statistically estimated (n > 350).

2.5. Colloidal stability evaluation

Particle size and ζ-potential determinations were performed using a Malvern Nano-ZS, Zetasizer Nano series. Around 1 mg of **ZnBDP_OH** was dispersed in 10 mL of different solvents (*i.e*. MilliQ water, ethanol and DMF) using an ultrasound tip (Digital Sonifer 450, Branson; from 10 to 20% of amplitude and for 30 s to 1 min).

Colloidal stability was also studied under relevant physiological conditions. Initially 2 mg of **ZnBDP_OH** were dispersed in 10 mL of MilliQ water by sonicating for 1 minute at 10%. Then, this colloidal solution was half-diluted by adding different media prepared as a double of the final concentration: simulated intestinal fluid (SIF),[43] diluted SIF (1/25, *lis*-SIF), diluted SIF supplemented with pancreatin (1% and 0.1% w/v) or mucin (0.5% and 0.05% w/v), PBS and PBS implemented with bovine serum albumin (BSA) (5.4% w/v). After mixing the **ZnBDP_OH** water solution with the above mentioned media, no more sonication treatment was applied in order to evaluate the evolution of the colloidal stability. In all cases, the final concentration of **ZnBDP_OH** was 0.1 mg mL^{-1}. All kinetic studies were carried out a by triplicate (n = 3) at 37 ºC and different times (*in situ* during the first 10 minutes and *ex situ* at 0.5, 1, 2, 4, 6, 8, 10 and 24 h). During the colloidal stability test, the ζ-potential as well as the crystallinity of the samples was monitored at different times.

pH titration curves. The effect of pH on the colloidal stability of the **ZnBDP_X** series was studied by suspending 10 mg of desolvated **ZnBDP_X** in 100 mL of MilliQ water (0.1 mg mL^{-1}). PH measurements were performed using a pH-meter (Thermo Scientific ATI Orion, 8163). The pH was adjusted within the range from 1 to 12 using NaOH or HCl solutions (0.03 M). At different pH values, aliquots of the stirred suspension (1.5 mL) were dispersed with an ultrasound tip (using 10% amplitude for 1 minute). Size and ζ-potential evolution was monitored in triplicate at 25 ºC.

2.6. Structural stability tests

Chemical stability was checked by suspending 2 mg of **ZnBDP_X** nanoparticles in 1 mL of MilliQ water at different pHs. The resulting suspensions were kept on an orbital incubator shaker at 37 ºC. After one hour, nanoparticles were filtered and XRPD were recorded.

2.7. Cytotoxicity assessment of the H_2BDP_X linkers

The J774 cell line was maintained in RPMI 1640 medium supplemented with 10% of fetal bovine serum (FBS), glutamax® and 1% of antibiotic antimycotic solution. The cell line was grown at 37 ºC in a humidified 95% air and 5% CO_2 atmosphere. The cytotoxic activity of the linkers was evaluated using the MTT assay (MTT = 3-(4,5-dimethylthiazol-2-yl)-2,5-diphenyltetrazolium bromide). Prior to the assay, cells were seeded in 96-well plates at a density of 1000 cells *per* well and cultured for 24 h. Different concentrations of H_2BDP_X ligands were prepared with a final volume of 200 μL *per* well, in any case the final concentration of DMSO in the 96-well plate was higher than 0.5%. After 24 h, a solution of MTT (final concentration 0.5 mg mL^{-1}) was added in each well and the plates were incubated at 37 ºC in a 5% CO_2 atmosphere for 2 h. Then, 200 μL of DMSO was added to each well and the plates were read at λ = 540 nm. All the measurements were performed by triplicate.

2.8. RAPTA-C and mitoxantrone incorporation and release

Evacuation/activation of **ZnBDP_X** *(X = H, NH_2, NO_2 and OH).* Prior to the loading of RAPTA-C and mitoxantrone, the as-synthesized **ZnBDP_X** solids were outgassed (10^{-2} Pa) at 200 ºC for 12 h. Under these conditions, the complete removal of the solvent guest molecules was achieved in order to obtain empty pores ready for drug adsorption.

Chemical stability. **ZnBDP_H** chemical stability was checked in MeOH, in order to establish the potential use of this solvent in RAPTA-C and mitoxantrone encapsulation. 20 mg of activated **ZnBDP_H** were suspended in 40 mL of MeOH for 4 h. Then, the solid was filtered and XRPD measurements were performed.

RAPTA-C adsorption at 25 ºC. RAPTA-C solution (at 80% saturation) was prepared using methanol as solvent. RAPTA-C solid-liquid adsorption experiments were performed at 25 ºC by suspending 100 mg of the activated **ZnBDP_X** (X = H, NH_2, NO_2 and OH) into the drug solution (RAPTA-C:ZnBDP_X ratio 0.6:1). The mixture was kept under stirring for 4 h in order to assure that the equilibrium was reached. Then, each sample was filtered and washed with MeOH (3 x 10 mL). The amount of RAPTA-C incorporated into **ZnBDP_X** was indirectly calculated by monitoring the decrease of RAPTA-C UV band from the methanolic solutions. Using the Lambert-Beer law, the concentration of RAPTA-C in methanol was calculated from the maximum absorbance peaks at 338 nm and 466 nm. Moreover, the quantity of adsorbed RAPTA-C into the MOFs was confirmed by elemental and thermogravimetric analyses.

Mitoxantrone adsorption at 25 ºC. the same procedure as for RAPTA-C was followed. In this case, the concentration of the non-encapsulated mitoxantrone was calculated from the maximum absorbance peaks at 614 nm and 663 nm in methanol.

Mechanochemical incorporation of mitoxantrone in **ZnBDP_X** (X = H and NH_2). Different ratios of **ZnBDP_X** solids and mitoxantrone (1:0.5; 1:0.6; 1:0.7; 1:0.8; 1:0.9; 1:1 for X = H and 1:0.1; 1:0.2; 1: 0.3; 1:0.4; 1:0.5 for X = NH_2) were manually grounded in an agate mortar for 20 minutes. Afterwards, each mixture was washed with acetone until mitoxantrone was not detected in the washings.

Diffuse reflectance spectra were registered for the empty **ZnBDP_X** matrices, mitoxantrone and all the solids obtained by impregnation or mechanochemical process. The quantity of adsorbed mitoxantrone into the MOFs was determined by interpolation, as well as elemental and thermogravimetric analyses.

Measurement of the adsorption isotherm of RAPTA-C at 25 ºC. For the evaluation of the amount of RAPTA-C adsorbed into **ZnBDP_H**, the concentration of the remaining free metallodrug in solution was checked by UV-vis. RAPTA-C solid-liquid adsorption isotherm was measured at 25 ºC by suspending 10 mg of activated **ZnBDP_H** in 10 mL of methanolic RAPTA-C solutions at different concentrations (0.8, 1.7, 3.5, 4.3, 5.2, 6,.0, 6.9, 8.6 and 10.4 mM). In order to assure that equilibrium was reached, the suspension was kept under stirring for 4 h. Then, each sample was centrifuged in a Sigma 2-16P centrifuge at (4000 rpm / 10 minutes) to achieve the separation of **ZnBDP_H@RAPTA-C** from the solution. The amount of RAPTA-C incorporated into **ZnBDP_H** matrix was indirectly calculated monitoring the decrease on the RAPTA-C UV-vis band from the filtered solution.

*Attenuated Total Reflectance (ATR) for RAPTA-C and mitoxantrone identification***.** The total amount of RAPTA-C or mitoxantrone incorporated into **ZnBDP_X** (X = H, NH_2, NO_2 and OH) by impregnation was also quantified by ATR. In order to check the amount of RAPTA-C or mitoxantrone adsorbed into the porous matrix, a calibration curve was recorded. For that, different mixtures of **ZnBDP_X** (10 mg) and RAPTA-C or mitoxantrone (4, 8, 12 and 16 mg) were manually grounded and then deposited in the sample holder. Additionally, the drug-loaded samples, obtained by impregnation **ZnBDP_X@RAPTA-C** and **ZnBDP_X@Mitoxantrone**, were recorded. It should be highlighted that the IR maximum absorption bands selected for the calibration purposes were the ones in which RAPTA-C and mitoxantrone have a maximum of

adsorption, while **ZnBDP_X** do not adsorb: *i)* RAPTA-C: 971, 1100 and 1280 cm^{-1} for X = H; 805, 902 and 1280 cm^{-1} for X = NO_2; 971 and 976 cm^{-1} for X = NH_2; and 968 and 1100 cm^{-1} for X = OH; *ii)* mitoxantrone: 720, 1211 and 1462 cm^{-1} for X = H; and 983 and 1214 cm^{-1} for X = NH_2.

RAPTA-C delivery. The delivery of RAPTA-C in simulated body fluid (SBF) was studied at 37 ºC. SBF was prepared according to literature methods.[44] With this purpose, we prepared two solutions, A and B that were mixed before each experiment.

SOLUTION A (NaCl: 6.213 g L^{-1}, $NaHCO_3$: 5.948 g mL^{-1}, KCl: 0.450 g L^{-1}, $K_2HPO_4 \cdot 3H_2O$: 0.462 g L^{-1}, $MgCl_2 \cdot 6H_2O$: 0.622 g L^{-1}, Na_2SO_4: 0.144 g L^{-1}, HCl (1M): 0.85 mL L^{-1}).

SOLUTION B (NaCl: 6.213 g L^{-1}, $Na_2HPO_4 \cdot 2H_2O$: 0.498 g L^{-1}, $CaCl_2$: 0.584 g L^{-1}, HCl (1M): 0.85 mL L^{-1}).

The metallodrug delivery together with the H_2BDP_X leaching processes were studied by suspending 10 mg of **ZnBDP_X@RAPTA-C** (X = H, NH_2, NO_2 and OH) in 150 mL of SBF incubated at 37 ºC under stirring. Aliquots (2 mL) of the supernatant solution were analyzed by means of UV-vis at different times (10, 20, 30, 40, 50 min, 1, 1.5, 2, 2.5, 3, 3.5, 4, 5, 7, 9, 11, 16, 18, 20, 22, 24, 27, 31, 25 and 48 h); in order to determine the released amount of RAPTA-C and the kinetics of the process. The solutions were filtered using centrifuge tubes with a 30 kDa PES filter (4000 rpm / 1 minute). Then, both the solution and the solid were joined to the mother solution to keep a constant volume. In SBF, RAPTA-C maximum absorbance peaks were found at 323 and 441 nm. These peaks were attributed to the ruthenium complex [Ru(*p*-cymene)Cl(H_2O)(pta)] that is immediately obtained when RAPTA-C is hydrolyzed in aqueous solution.[45] H_2BDP_X ligands, eventually leached during RAPTA-C delivery, are slightly soluble in SBF. Nevertheless, their UV-vis maximum absorption bands were found at 224, 261 and 300

nm (H_2BDP), 252 nm (H_2BDP_NO_2), 300 nm (H_2BDP_NH_2) and 237 and 287 nm (H_2BDP_OH), and therefore, they cannot interfere with the UV-vis absorption of the RAPTA-C species.

Mitoxantrone delivery. On the other hand, mitoxantrone delivery was studied by suspending 20 mg of **ZnBDP_X@Mitoxantrone** (X = H and NH_2) in 40 mL of SBF. The resulting suspension was incubated at 37 ºC under stirring. Aliquots (2 mL) of the supernatant solution were analyzed by means of UV-vis at different times, during 24 hours; in order to determine the released amount of mitoxantrone and the kinetics of the process. As in RAPTA-C delivery study, the solutions were filtered using centrifuge tubes with a 30 kDa PES filter (4000 rpm / 1 minute).

3. RESULTS AND DISCUSSION

3.1. Synthesis of nanometric ZnBDP_X

The series of porous polycrystalline **ZnBDP_X** family (X= H, NH_2, NO_2 and OH)[25] materials are obtained by reacting zinc acetate with the organic linkers in boiling *N,N'*-dimethylformamide (DMF). To control the particle size and reduce the polydispersity, the kinetics of crystallization the **ZnBDP_X** solids was first investigated by *ex situ* XRPD, collecting samples at different reaction times. Interestingly, nanocrystalline **ZnBDP_H** and **ZnBDP_NO_2** were obtained after only 1-hour, whereas 2 hours were required to form the **ZnBDP_NH_2** and **ZnBDP_OH** derivatives (Figure S1). Moreover, the evolution of the particle size was studied as a function of time (from 1 to 7 h) using a combination of different techniques (Scherrer's equation from XRDP data (eq. (1); see experimental section), FEG-SEM images and DLS measurements; Table 1). The mean size of the crystalline domains estimated by the Scherrer's law remained in the nanometric range with particle sizes of ~50 nm. It is noteworthy that the nanosize of the crystalline domain was kept up to 7 h, indicating no evolution of crystallinity with time. After 7 h of reaction, FEG-SEM images showed tetragonal particles with mean sizes of *ca*. 65 nm for **ZnBDP_H**, –**NO_2** and –**OH** and more elongated particles with slightly larger size (*ca.* 120 x 45 nm) for **ZnBDP_NH_2** (Figure S2). These values are in good agreement with the values deduced from XRPD, indicating that the particle is formed by a unique crystalline domain with no additional growth after 1 h of reaction. In addition, there was an increase of the reaction yields (from ~45 to ~60%) with time (Table 1). This suggests that the general mechanism of nucleation of these nanoparticles should involve the growth of novel crystal nuclei from the homogeneous phase. Moreover, the obtained yield values can be considered high enough for the synthesis of

MOF nanomaterials.[46,47] However, the larger particle sizes (100-200 nm), determined in solution by DLS, suggest aggregation processes in the liquid medium (*i.e.* DMF). However, it should be highlighted that with the exception of **ZnBDP_H**, the size of the aggregates remained constant along the reaction time (up to 7 h) with a low degree of polydispersity (indices (PDI) < 0.3; Table 1). In contrast, for pristine **ZnBDP_H**, a progressive and significant increase of particle size from 100 ± 15 to 180 ± 25 nm was observed together with higher PDIs (*ca*. 0.5; Table 1).

Table 1. Particle size (estimated using the Scherrer's equation (XRPD), SEM images and DLS measurements (including polydispersity index, PDI)) of **ZnBDP_X** series, prepared by conventional synthesis, as a function of the reaction time. The yield of the reactions at 2, 4 and 7 hours is also displayed.

		Reaction time (h)	1	2	3	4	5	6	7
ZnBDP_H	Size (nm)	DLS (PDI)	105 ± 15 (0.4)	150 ± 20 (0.5)	145 ± 15 (0.5)	155 ± 30 (0.5)	140 ± 20 (0.5)	170 ± 25 (0.6)	180 ± 25 (0.5)
		XRPD	46	47	50	51	60	50	52
		SEM							70 ± 24
	Yield (%)			53		53			57
ZnBDP_NH$_2$	Size (nm)	DLS (PDI)	190 ± 35 (0.2)	210 ± 30 (0.1)	193 ± 40 (0.1)	220 ± 35 (0.2)	210 ± 35 (0.1)	210 ± 35 (0.1)	275 ± 35 (0.1)
		XRPD	-	58	71	67	65	71	61
		SEM							120 ± 40 & 45 ± 20*
	Yield (%)			45		46			58
ZnBDP_NO$_2$	Size (nm)	DLS (PDI)	125 ± 35 (0.3)	100 ± 30 (0.3)	120 ± 25 (0.3)	120 ± 30 (0.3)	115 ± 30 (0.2)	100 ± 30 (0.2)	120 ± 35 (0.3)
		XRPD	45	43	42	39	-	37	39
		SEM							65 ± 30
	Yield (%)			48		58			62
ZnBDP_OH	Size (nm)	DLS (PDI)	145 ± 35 (0.2)	145 ± 35 (0.2)	160 ± 30 (0.2)	165 ± 35 (0.2)	165 ± 35 (0.2)	160 ± 35 (0.2)	155 ± 40 (0.2)
		XRPD	52	50	45	45	40	34	50
		SEM							60 ± 20
	Yield (%)			35		47			63

*length and width respectively

Alternatively, in an attempt to avoid the use of toxic DMF as solvent, an environmentally friendly microwave-assisted solvothermal route using propan-2-ol as solvent was investigated to prepare **ZnBDP_OH** nanoparticles. This microwave route might also lead to a reduction of the temperature and reaction time, affording improved synthetic conditions. With this aim, several Zn precursors were initially screened ($Zn(AcO)_2$, Zn(2,4-pentanedionate)$_2$, $ZnCl_2$ and $Zn(NO_3)_2 \cdot 6H_2O$). In contrast with $ZnCl_2$ and $Zn(NO_3)_2 \cdot 6H_2O$, leading to the formation of amorphous products, $Zn(AcO)_2$ and Zn(2,4-pentanedionate)$_2$ led to the pure **ZnBDP_OH** structure, as demonstrated by XRPD (Figure S3). Note here that reaction times of 24 h were required in order to obtain the pure phase in propan-2-ol using the traditional conventional electric heating synthesis while, when using microwave, only 1 h was required for the preparation of **ZnBDP_OH** phase avoiding the presence of impurities. In addition, important yields (ca. 78% *vs* 63% for the conventional synthesis in DMF) were thus achieved using lower temperatures (100 *vs*. 150°C) than using the conventional synthetic method in DMF (Figure S3). DLS measurements in propan-2-ol of the **ZnBDP_OH** synthesized from $Zn(AcO)_2$ or Zn(2,4-pentanedionate)$_2$ precursors showed however a larger particle size, reaching 775 ± 85 nm (PDI = 0.3) and 290 ± 25 nm (PDI = 0.6), respectively. However, **ZnBDP_OH** nanoparticles synthesized from propan-2-ol and later dispersed in DMF give rise to smaller particle size, namely, *ca.* 191 ± 21 nm, in agreement with a higher aggregation in propan-2-ol.

The crystalline domain extracted from Scherrer equation (eq. (1)) and FEG-SEM images of **ZnBDP_OH** (obtained using Zn(2,4-pentanedionate)$_2$ as a precursor) confirmed the presence of small faceted nanoparticles with a particle size of *ca*. 85 ± 25 nm (Figure S4), not that different from those synthesized in DMF under reflux (60 ± 20 nm). These results confirm the possibility

of synthesizing small **ZnBDP_OH** nanoparticles (~85 nm) by using a totally green microwave synthetic route, compatible with biomedical applications, in only 1 h of reaction.

Interestingly, **ZnBDP_OH** material could also be obtained using the environmentally friendly propan-2-ol under reflux in absence of any pressure. However, the pure phase was only achieved after 24 hours reaction time, as demonstrated by XRPD (Figure S3).

3.2. Colloidal stability of **ZnBDP_X** in different media

To shed some light on the understanding of the colloidal stability of **ZnBDP_OH**, desolvated nanoparticles were dispersed in different solvents (MilliQ water, ethanol and DMF) and their particle size and ζ-potential monitored (see experimental section; Table S1). The desolvated **ZnBDP_OH** nanoparticles were easily dispersed in all solvents by optimizing the sonication conditions, leading to similar dimensions (~100-140 nm) than those measured from the as-synthesised DMF sample. However, considering the initial aggregation of these nanoparticles (60 *vs.* 140 nm as determined by FEG-SEM/XRPD and DLS, respectively), the redispersion in solvents did not lead, whatever the conditions, to smaller nanoparticles, indicating that the initial aggregation state is hard to overcome.

Aside from particle size, the nature of the nanoparticle surface will determine the interaction with the different components of the physiological media (solvent molecules, ions, proteins, enzymes, lipids, etc.). In this respect, it is commonly admitted that nanoparticles exhibiting a ζ-potential value higher than ± 30 mV are stable in suspension.[48] It should also be highlighted that a negatively charged surface is critical to minimize protein adsorption and, consequently to afford stealth properties to the nanoparticles. On the other hand, cationic nanoparticles are believed to be more toxic and induce higher inflammatory reactions than negatively charged

ones.[49] Interestingly, **ZnBDP_OH** nanoparticles exhibited a negative surface charge of *ca.* -20 mV regardless the solvent (Table S1). The external surface of **ZnBDP_OH** might be composed of octahedral Zn species, whose coordination sphere may be typically completed by hydroxide, water moieties or pyrazolate linkers. Considering the negative charge of **ZnBDP_OH** nanoparticles and the high pKa of the pyrazolate and hydroxyl groups (~20 and ~10, respectively), this rules out any deprotonation of the organic spacer in pure water (pH ~6), indicating the presence of mainly inorganic moities on the outer surface. Finally, all the samples showed a complete preservation of their crystalline structure (Figure S5), evidencing not only a high colloidal stability but also a structural and chemical robustness within MilliQ water, DMF and EtOH.

To get a better insight into the structural and colloidal stability of **ZnBDP_OH** nanoparticles in aqueous media, the evolution of the particle size was followed during longer times (24 h) and at different pHs (from 1 to 12). Note here that the biological media are generally based on aqueous solutions at different pHs. A 24 h-kinetics of the colloidal stability study in MilliQ water did not show any significant variation on either size of the nanoparticles (110 ± 20 nm), polydispersity (0.5), or ζ-potential (-18 ± 1 mV) (Figure S6, Table 2), making these nanoparticles promising nanocarriers for *in vivo* applications. In contrast, previous results obtained using the benchmarked MIL-100(Fe) nanoparticles showed a much lower colloidal stability, associated with an aggregation phenomenon after 6 h when dispersed in MilliQ water, reaching micrometric sizes after 24 h.[15] The higher colloidal stability of **ZnBDP_OH** nanoparticles could be explained by their different chemical nature: a higher stability of pyrazolate- *versus* carboxylate-based MOFs (pka ~20 and ~4, respectively) in water, particularly when the pH increases, and a different surface chemistry, which would prevent from aggregation. Nevertheless, structural

stability monitored by XRPD experiments indicated a progressive loss of crystallinity, with an almost complete amorphization after 24 h (Figure S7). The progressive degradation, with a concomitant weight loss of approximately a third of its initial mass is attributed to the release of BDP_OH polar ligands and the formation of amorphous zinc hydroxide (see below).

On the other hand, when the **ZnBDP_OH** matrix is exposed at different pHs, the particle size is still kept almost constant (~ 100 nm) (Figure S8(d)). Similarly, ζ-potential remains negative in almost all the pH range (> 2.5), with an isoelectric point (pI) at *ca*. 2.2. While the higher negative charges (~ -40 mV) observed at pH > 9 could be related with the deprotonation of the OH group (BDP–OH / BDP–O^-; pka ~ 10 considering Ph–OH), the positive ζ-potential values at lower pHs (< 2.5) (Figure S8(d)) could be associated with the framework degradation, as evidenced by XRPD (Figure S9). According to the Pourbaix diagram,[50] we can tentatively conclude that there is an destabilization of the structure, through the formation of soluble Zn^{2+} species, under strong acidic conditions (pH = 1.2, *i.e.* gastric conditions), while at very high pH (pH = 12) only a partial degradation of the nanomaterial takes place due to the formation of zinc oxide. This is in agreement with the pH responsive behaviour of the Zn imidazolate ZIF-8 with a faster degradation of the framework when the pH becomes more acidic.[51] In summary, **ZnBDP_OH** matrix shows a relatively high structural stability under a wide pH range.

Finally, the effect of pH on the ζ-potential and particle size of the other functionalized **ZnBDP_X** matrices was also investigated (Figure S8). Remarkably, the colloidal stability is strongly affected by the functionalization of the organic linker. While **ZnBDP_OH** suspension is highly stable over all the pH range, **ZnBDP_H**, **ZnBDP_NO_2** and **ZnBDP_NH_2** show significant aggregation within the 4-9, 1-3 and 3-4 pH ranges, respectively (Figure S8). The overall evolution of the ζ-potential however follows a similar profile for all the **ZnBDP_X**

nanoparticles: *i)* neutral charges at very low pHs (pI < 2.7); *ii)* positively charged surfaces below this pI (from +8 to +25 mV for **ZnBDP_NH$_2$** and **ZnBDP_OH**, respectively), probably due to the framework degradation at highly acidic pHs (*i.e.* gastric conditions; see XRPD Figure S9); *iii)* negative surfaces at pH > pI with different net ζ-potential values, depending on the functional group; and finally *iv)* highly negative ζ-potential values (from -40 to -50 mV) under strongly basic conditions (11 – 12). One could tentatively assign this to the formation of zinc hydroxide species on the surface of the nanoparticles. These highly negatively charged surfaces are associated to sufficient electrostatic repulsive forces to prevent nanoparticles from aggregation, leading to stable colloidal solutions with a particle size smaller than 150 nm.

Therefore, both particle size and ζ-potential are strongly modified by the functional group within the pH range from 2 to 9. In **ZnBDP_NH$_2$** and **ZnBDP_NO$_2$**, at pHs near to the pI, nanoparticles aggregate, giving rise to maximum particle sizes of 422 ± 100 and 673 ± 135 nm, respectively. This could be explained taking into account the low net ζ-potential values (-11 and -7 mV, respectively), suggesting that electrostatic repulsive forces might be insufficient to prevent nanoparticles from aggregation. At pH > 4, higher net ζ-potential values are observed (from -10 to -20 mV at pH = 4 and 9, respectively) and, as a consequence, the electrostatic repulsive forces are stronger than the van der Waals attractive forces. Then, nanoparticle aggregation is hindered and particle size decreases to ~100 nm (Figure S8). Considering the majority presence of Zn units on the surface and based on the zinc chemistry in solution,[52] this might correspond to the formation of Zn hydroxide species at higher pHs. The **ZnBDP_OH** analogue, shows an even more negative ζ-potential values (from -20 to -30 mV at pH = 4 and 9), which ensure further stabilize the colloids throughout this pH range. Although the hydroxyl groups could be involved in the stabilization of the colloids at higher pHs (> 9), the weak acidic

character of this group (pKa~ 10 for Ph–OH) rules out any protonation at pH ≤ 9 that would improve the colloidal stability. It is noteworthy that the important polarity of –OH groups, as well as the $–NH_2$, could influence the stability of colloids through hydration phenomena. This hypothesis is supported by the colloidal instability of the hydrophobic **ZnBDP_H** within a large range of pH (from 1 to 9), where submicronic aggregates are observed (from 228 nm at pH = 3 to 857 nm at pH = 6) associated to low net ζ-potential values close to zero (from -10 to +10 mV). In summary, the introduction of hydrophilic groups on the BDP linkers improve their aqueous colloidal stability. This provides an additional advantage if one considers that polar compounds are more soluble and thus often easily excreted from the body. For these reasons, and together with the possibility to produce homogeneous nanoparticles through a biofriendly method, we have selected the **ZnBDP_OH** analogue to further evaluate its colloidal stability in different simulated physiological conditions.

3.3. Colloidal stability of **ZnBDP_OH** under relevant physiological conditions

In order to confirm the potential of these nanomaterials to be used as carriers for *in vivo* applications, the stability of **ZnBDP_OH** nanoparticles was evaluated under experimental conditions that simulate those encountered in the two most widely used drug administration modes: intravenous and oral.

Simulated intravenous conditions. Although invasive and requiring the assistance of trained staff, this route acts very rapidly and essentially ensures a 100% bioavailability (excluding protein binding, degradation, etc). Considering the composition of the serum,[53] the structural and colloidal stability of **ZnBDP_OH** was studied in two different media at 37°C for 24 h: *i)* PBS (138 mM NaCl, 2.74 mM KCl and 10.0 mM Na_2HPO_4/NaH_2PO_4, pH = 7.4), considering that

phosphates might even at low concentration compete with the the azolate for the coordination of on the metal cation leading to destabilization and/or degradation effects, and *ii)* PBS supplemented with bovine serum albumin (BSA, 5.4% w/v), the most abundant plasma protein in mammals, which can also play an important role in the colloidal stability of nanoparticles under intravenous conditions.[54,55] Note that albumin concentration was in the upper level usually found in human physiological conditions (*i.e*. 3.5 – 5.0% w/v) in order to better observe the impact of the albumin over the colloidal stability.

At short times, **ZnBDP_OH** nanoparticles display a larger size and polydispersity index in PBS (200 ± 25 nm; PDI = 0.9) compared to MilliQ water (110 ± 25 nm and PDI = 0.6; Table 2). In addition, in contrast with the high 24 h-colloidal stability of **ZnBDP_OH** nanoparticles in pure water, a slow and progressive aggregation is observed in PBS (from ~200 to ~400 nm after 24 h; Figure 2 and Table 2). This might be related to a certain decrease in the net value of ζ-potential from -22 to -8 mV in MilliQ water and PBS, respectively. This suggests that the system becomes unstable because the presence of phosphate electrolytes on the surface causes the reduction of the electrostatic repulsion between two neighbouring nanoparticles, in agreement with the DLVO theory.[56]

Interestingly, the presence of albumin in the PBS medium leads to a stabilization of the colloidal solution up to 24 h (Figure 2). The lower particle size of **ZnBDP_OH** in PBS+BSA compared with PBS medium would be in agreement with the deposition of the protein at the external surface of nanoparticles. One could tentatively suggest the formation of specific interactions between the surface zinc cations and reactive groups of amino acids ($–NH_2$ and –COOH), among others. In fact, the negative ζ-potential can be attributed to the protein corona, as albumin is negatively charged at pH 7.4 (pI = 4.7).[57] Although the similar and quite neutral ζ-

potential values in PBS (~ -8 mV) and PBS+BSA (~ -9 mV) (Table 2) exclude at first sight stabilization *via* electrostatic repulsions, one can suggest the steric hindrance provided by the protein corona as the origin of the improved colloidal stability of **ZnBDP_OH**, in agreement with previously reported results.[15] Taking into account that albumin is the main protein present in plasma and, consequently, the major component of the protein corona just after the intravenous administration of nanoparticles,[58,59] these results suggest that the formation of a protein corona upon **ZnBDP_OH** intravenous administration should ensure a suitable colloidal stability in the serum medium. Finally, it should be also noted that the large volume of BSA (ellipsoid of around 4 x 14 nm)[60] rules out its adsorption within the MOF pores (1.1 nm pore diameter), preserving intact their porosity as well as *a priori* its cargo.

Table 2. Particle size (nm) and ζ-potential (mV) of **ZnBDP_OH** nanoparticles under different simulated physiological conditions at 37 ºC.

	Size (nm)		**ζ-Potential (mV)**	
Medium	**30 s**	**24 h**	**30 s**	**24 h**
MilliQ	110 ± 25	110 ± 25	-22 ± 2	-18 ± 1
PBS	200 ± 25	400 ± 130	-8 ± 2	-14 ± 3
PBS + BSA 5.4%	130 ± 30	175±70	-9 ± 3	-12 ± 1
HCl pH 1.2	192 ± 65	-#	-13 ± 5	-#
SIF	90 ± 15	130 ± 50*	-15 ± 3	-14 ± 3
lis-SIF	115 ± 1	105 ± 10	-18 ± 2	-31 ± 2
lis-SIF + Pancreatin 0.1%	160 ± 5	350 ± 70	-13 ± 3	-15 ± 3
lis-SIF + Pancreatin 1.0%	510 ± 30	>1000	-9 ± 2	-11 ± 1*
lis-SIF + Mucin 0.05%	410 ± 70	80 ± 40	-16 ± 3	-10 ± 1

*Values after 2 h of incubation

The colloidal stability of ZnBDP_OH under gastric conditions (pH = 1.2, 37 ºC) over 24 h could not be investigated as our system undertakes a rapid degradation in this highly acidic medium

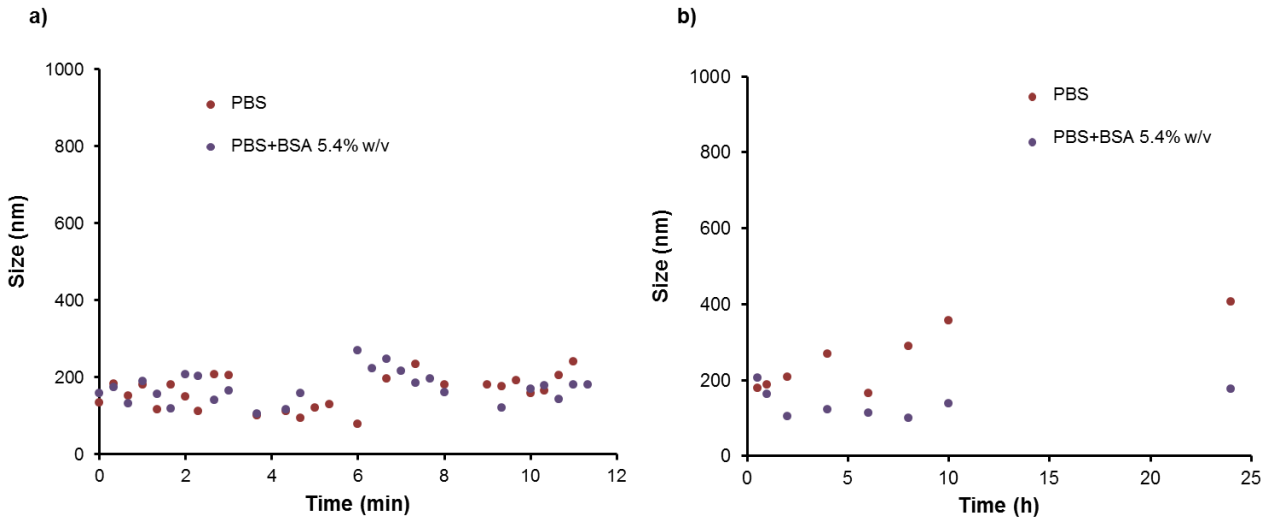

Figure 2. (a) Short-term (10 min) and (b) long-term (24 h) regime aggregation kinetics of ZnBDP_OH nanoparticles at 37 ºC in PBS (red) and PBS+BSA (5.4% w/v) (purple). For the sake of clarity, error bars have been removed from the plots (available in the Supporting Information, Figure S10).

On the other hand, the structural integrity of **ZnBDP_OH** nanoparticles was confirmed by XRPD after their suspension in the above mentioned physiological media over 24 h (Figure S11). A partial chemical degradation is however noticed, associated with a material degradation of around 14.5 and 33% in PBS and PBS+BSA, respectively, attributed to BDP_OH release (see above).

Simulated oral conditions. While parenteral route provides immediate onset of action, oral administration of medicines is preferred as it is less expensive and invasive for the patients. However, it is considered that the use of nanoparticles as efficient drug delivery systems is often blocked by the enzyme activity and the mucus barrier (gastric, intestinal, etc.). Therefore, nanoparticles must efficiently overcome these natural barriers to avoid rapid clearance.[61] In this context, the stability of **ZnBDP_OH** suspensions was studied upon exposition to similar conditions as those encountered through the digestive tract. To this aim, short- (10 min) and

long-term (24 h) regime experiments were performed under different conditions: *i)* simulated intestinal fluid, SIF (50.0 mM KH_2PO_4 and 15.4 mM NaOH at pH 6.8, 37 °C), *ii)* low-ionic-strength SIF, *lis*-SIF (diluted 1/25) and *iii) lis*-SIF supplemented with pancreatin (0.1% and 1% w/v), a mixture of digestive enzymes comprising amylases, lipases and proteases. The use of *lis*-SIF instead of SIF prevents the salt-induced destabilization of the system, by reducing the concentration of electrolytes, and allows the discrimination of the effect of the pancreatin on the colloidal stability of the suspension. Finally, the potential interaction of **ZnBDP_OH** with intestinal mucosa was analyzed by the incubation in *lis*-SIF supplemented with mucin (0.5 and 0.05% w/v), the main structural component of the intestinal mucus acting as a protective barrier. It should be noted that the study of the colloidal stability of **ZnBDP_OH** under gastric conditions (pH = 1.2, 37 ºC) over 24 h could not be investigated as this system suffers from a rapid degradation in this highly acidic medium according to XRPD (see section 3.3, Figure S9). However, for future applications, the instability of **ZnBDP_OH** nanoparticles in gastric conditions could be overcome using gastro-resistant capsules or coatings that prevent from degradation until de intestinal track is reached.

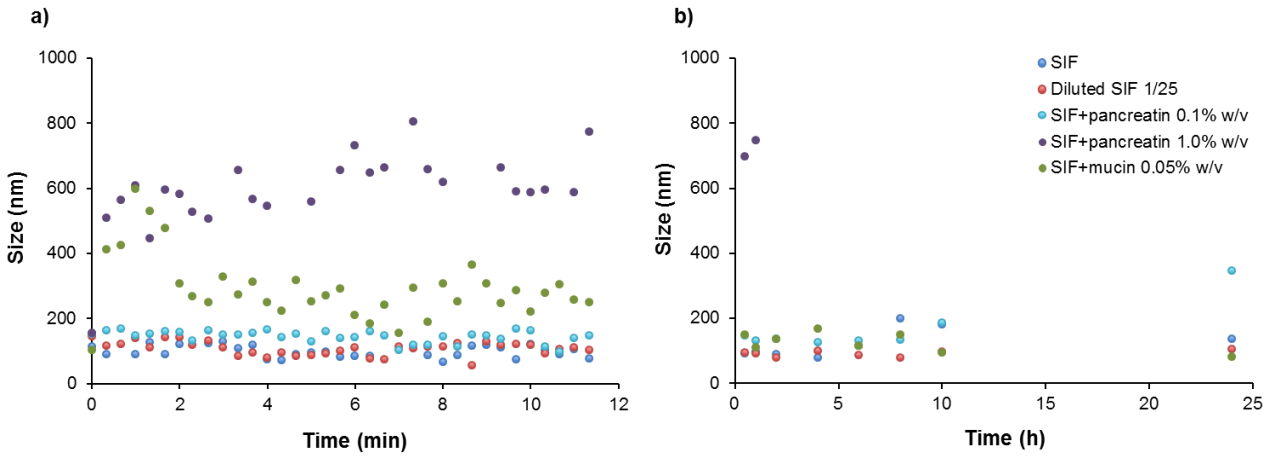

Figure 3. (a) Short- (10 min) and (b) long-term (24 h) regime aggregation kinetics of **ZnBDP_OH** nanoparticles at 37 ºC in SIF (dark blue), *lis*-SIF (diluted SIF 1/25, red), *lis*-SIF + pancreatin (0.1% w/v)

(light blue), *lis*-SIF + pancreatin (1% w/v) (purple) and *lis*-SIF + mucin (0.05 % w/v) (green). For the sake of clarity, error bars have been removed from the plots (available in the Supporting Information, Figure S12).

At shorter times (10 min), excepted the 1.0% w/v-pancreatin supplemented *lis*-SIF solution, **ZnBDP_OH** nanoparticles showed a high colloidal stability in all tested simulated intestinal fluids regardless the presence of mucin or low concentrated-enzymatic (0.1% w/v) fractions. Furthermore, small (~ 100 nm) and polydisperse (PDI from 0.6 (0.1% w/v pancreatin) to 1 (SIF)) nanoparticles were observed at longer times, which exhibited only slight changes in their mean size (~ 20 nm) over 10 h (Figure 3(b)). In fact, several aspects can be highlighted concerning the colloidal stability of **ZnBDP_OH** under intestinal fluids. First of all, and in contrast with the lower colloidal stability in PBS, which afforded aggregated particles of 400 ± 130 nm after 24 h (Figure 2(b)), the higher stability of the **ZnBDP_OH** in *lis*-SIF media (also based on a phosphate buffer) may be attributed to the lower ionic strength of this medium in comparison with PBS (2.6 *vs*. 150 mM). This is in agreement with the net surface charge of the nanoparticles since it is well known that an increase in ionic strength of the solution decreases thickness of electrical double layer, leading to a decrease in ζ-potential.[62] For instance, after 24 h a ζ-potential of -31 ± 2 and 14 ± 3 mV are obtained in *lis*-SIF and PBS, respectively, supporting the higher colloidal stability of **ZnBDP_OH** in this low-salt concentrated SIF medium (Table 2, Figure S13).

Second, the presence of pancreatin (0.1% and 1% w/v) strongly affects the colloidal stability of **ZnBDP_OH** in *lis*-SIF, depending on its concentration (Table 2, Figure 3). While in *lis*-SIF + 0.1% pancreatin medium, the colloidal solution was stable up to 10 h with a slight aggregation at 24 h (346 ± 73 nm), an important aggregation process was detected in *lis*-SIF + 1.0% pancreatin at short times (510 ± 30 nm at 30 s) reaching particle sizes up to ~800 nm after only 2 h of

incubation. This might be related with a reduction of the ζ-potential in presence of pancreatin from the very beginning (from -18 to -9 mV in *lis*-SIF and *lis*-SIF + 1.0% pancreatin, respectively), following a concentration-dependent tendency. This suggests the formation of an enzyme coating on the outer surface of **ZnBDP_OH** nanoparticles. In addition, considering the surface charge evolution of **ZnBDP_OH** in *lis*-SIF (from -18 ± 2 to -31 ± 2 mV) and the lack of an important time evolution of the ζ-potential values in the pancreatin coated nanoparticles (from -13 ± 3 to 15 ± 3 mV in *lis*-SIF+0.1% pancreatin and from -9 ± 2 to -11 ± 1 mV in *lis*-SIF+1.0% pancreatin), one could consider that the enzyme corona is kept along time (Table 2, Figure S13). This could be related with the interaction between the nanoparticle surface and the enzyme fraction (proteins), possessing reactive groups able to strongly coordinate the zinc on the surface. However, the different behavior observed in *lis*-SIF + 1% pancreatin solutions can be attributed to the presence of depletion forces induced by the crowd protein environment.[63] It is known that bridging and depletion phenomena depend on the ionic strength of the medium and the charge of the emulsifier.[64] Between 0.1 and 1 % pancreatin solution there is a 10-fold increment on the ionic strength that could explain the different colloidal behaviour.

It should be noted that the dispersion of **ZnBDP_OH** in *lis*-SIF supplemented with 0.5% mucin led to a rapid increase in size, giving rise to > 1 micron aggregates in less than 1 minute (Figure S14). This result indicates that **ZnBDP_OH** nanoparticles are able to interact with mucin (usually at 2-5% in healthy human intestine),[65] suggesting a certain degree of adhesion, potentially associated with a longer retention in the intestinal mucosa after oral administration. To further understand this effect, we used more diluted mucin supplemented *lis*-SIF media (0.05 % w/v), evidencing an initial aggregation of nanoparticles (300-600 nm at t ≤ 10 min), in agreement with a potential interaction of **ZnBDP_OH** with the mucin (Table 2, Figure 3(a)).

However, at longer times (30 min > t > 24 h), particle size decreases, associated to disaggregation phenomenon, reaching similar dimensions than the initial product (around 100 nm) with no variation along time (Figure 3(b)). As occurred in the medium supplemented with pancreatin, the net ζ-potential value after 24 h decreases from - 16 ± 3 to - 10 ± 1 mV, suggesting the covering of the outer surface of **ZnBDP_OH** nanoparticles by mucin residues (Table 1, Figure S13). The well known tendency of other substances to adhere to mucin is not surprising given that this glycoprotein exhibits electrostatic, hydrophobic and H-bonding interactions.[66] Taking into account the presence of negatively charged groups (carboxyl or sulphate)[67] on the mucin surface, **ZnBDP_OH** nanoparticles might interact with these groups at the interface through hydrogen bonds, which will further explain the decrease of net ζ-potential value.

Finally, the preservation of the crystalline structure of this material was evidenced under the tested intestinal conditions after 24 h by XRPD (Figure S15). However, a slight peak broadening attributed to the partial degradation of the porous matrix under these conditions was noticed. Larger peak broadening seems to be detected in SIF and *lis*-SIF, being consistent with a higher instability, in agreement with the previous results in PBS. Interestingly, **ZnBDP_OH** seems to be more stable in *lis*-SIF media supplemented with pancreatin or mucin, supporting the formation of a protein-corona on the nanoparticles' surface, which could protect them from degradation in the presence of salts, as previously demonstrated for the MIL-100(Fe) nanoparticles under similar conditions.[15]

3.4. Incorporation and release of the RAPTA-C and mitoxantrone into **ZnBDP_X**

In order to evaluate the potential application of the **ZnBDP_X** series (H_2BDP_X = 1,4-bis(1H-pyrazol-4-yl)2-X-benzene, X= H, NO_2, NH_2 and OH) as drug carriers, we initially study the

biocompatility of these nanoparticles. Considering the endogenous character of the zinc, as well as its important human daily requirements (8-14 mg),[68] high lethal dose 50 (oral LD50= 3 g kg^{-1}) and easy fecal excretion,[69] zinc seems to be a biocompatible cation. On the other hand, the *in vitro* cytotoxicity of H_2BDP_X ligands was experimentally evaluated on murine macrophages cell line (J774) using the MTT assay. The cytotoxicity tests confirmed that the H_2BDP_X ligands exhibited a certain degree of cytotoxicity, since cellular viability values were reduced (< 24%) when the macrophages were incubated using a ligand concentration of 20 μg mL^{-1} for 24 hours. This result is in contrast with the low toxicity reported for other ligands used for the construction of MOFs with drug delivery properties (i.e. fumaric acid, IC_{50} = 10 g Kg^{-1}; trimesic acid, IC_{50} = 8.4 g Kg^{-1}; terephthalic acid, IC_{50} = 6.4 g Kg^{-1})[70,71]. However, it should be noted that there are other proposed drug delivery systems exhibiting a similar toxicity than H_2BDP_X ligands (Mg-Al-LDH (IC_{50} = 20 μg mL^{-1}, colon cells),[72] CdTe QD (IC_{50} = 10 μg mL^{-1}, MCF-7 cells),[73] AE-SNEDDS (using a concentration of μg mL^{-1} less than 45% cell viability was observed in Caco-2 cell line).[74] Furthermore, concerning cancer treatment, traditional chemotherapeutic agents are cytotoxic (mitoxantrone (IC_{50} = $5.4 \cdot 10^{-3}$ μg mL^{-1}, juveniles of Daphnia magna),[75] *cisplatin* (IC_{50} = 0.022 μg mL^{-1}, KLE cells), *carboplatin* (IC_{50} = 0.096 μg mL^{-1}, KLE cells).[76] This means that the possible cytotoxicity of the **ZnBDP_X** porous matrices might be tolerated versus the benefit of healing. Nevertheless, the impact of ligand cytotoxicity will depend on the structural stability of the porous matrix **ZnBDP_X** under physiological conditions. Taking into account all of these considerations, it will be interesting to extend these toxicity studies to the porous matrices in a near future.

In a second step, the encapsulation of the non-conventional antitumor drugs (RAPTA-C and mitoxantrone) was carried out in the **ZnBDP_X** series by impregnation. The drugs were

incorporated in **ZnBDP_X** (X = H, NO_2, NH_2 and OH) by suspending the previously activated matrices in drug-saturated methanol solutions for 4 h. The suspensions were then filtered and solids were cleaned and analyzed so as to determine the drugs adsorption into the MOF series. The results obtained by elemental and thermogravimetric analyses (see supplementary information), UV-vis and attenuated total reflectance (ATR) confirmed the successful incorporation of the metallodrug RAPTA-C in all the porous matrices (Table 3, Figure S17). Noteworthy, RAPTA-C adsorption capacity in **ZnBDP_X** series follows the same trend than the surface area of the solids (Table 3), with a loading capacity mainly depending on the accessibility of the porous network. However, in the case of mitoxantrone, drug incorporation was only achieved for **ZnBDP_X** (X = H and NH_2) derivatives (Table 3, Figure S18). A plausible explanation might be related to an adequate balance between pore accessibility, framework flexibility and affinity of the pore surface for mitoxantrone, which would favour its incorporation in **ZnBDP_X** (X = H and NH_2). The structural integrity of the **ZnBDP_X** series after the drug loading process was studied using XRPD, revealing that the diffraction patterns of the loaded-MOFs significantly change from the initial activated ones (Figure S20). XRPD **ZnBDP_X@RAPTA-C** and **ZnBDP_X@Mitoxantrone** materials show similar XRPD patterns than the freshly prepared materials loaded with DMF molecules **ZnBDP_X@DMF**. These results confirm the flexible behaviour of the matrices, since they can accommodate guest molecules by simple stretch and shrinkage of their porous structure, affecting the XRPD patterns, with changes in cell volume and symmetry.[77] Similar flexible and versatile properties were recently described on the CoBDP structure during the incorporation and delivery of solvent molecules,[78] and in the porous matrix MIL-53 in the adsorption and release of guests (*e.g.* ibuprofen).[79]

Table 3. Loading by impregnation of RAPTA-C and mitoxantrone anticancer drugs in the series **ZnBDP_X** (mmol of drug *per* mmol of nanomaterial). Dramatic reduction of the adsorption capacity and the pore volume of the drug-loaded MOFs.

	ZnBDP_H	**ZnBDP_NO_2**	**ZnBDP_NH_2**	**ZnBDP_OH**
RAPTA-C (mmol $mmol^{-1}$)	0.55	0.22	0.11	0.15
Mitoxantrone (mmol $mmol^{-1}$)	0.50	-	0.20	-
S_{BET}* (m^2 g^{-1})	2450	2280	1420	1020
S_{BET} (m^2 g^{-1}) (RAPTA-C loaded matrices)	95	30	140	215
S_{BET} (m^2 g^{-1}) (Mitoxantrone loaded matrices)	40	-	60	-
Pore volume (cm^3 g^{-1})RD	0.959	0.822	0.677	0.516
Pore volume (cm^3 g^{-1})RD (RAPTA-C loaded matrices)	0.045	0.013	0.119	0.101
Pore volume (cm^3 g^{-1})RD (Mitoxantrone loaded matrices)	0.019	-	0.123	-

RD: Using Dubinin-Radushkevitch equation[80]

*BET: according to the Brunauer-Emmett-Teller theory

On the other hand, the reported incorporation of these anticancer drugs within the cavities of the nanoMOFs series **ZnBDP_X** is related with the dramatic reduction of the adsorption capacity of the MOFs, where the BET surface drops from 2450 m^2 g^{-1} (**ZnBDP_H**) to 95 m^2 g^{-1} (**ZnBDP_H@RAPTA-C**) and 40 m^2 g^{-1} (**ZnBDP_H@Mitoxantrone**); from 2280 m^2 g^{-1} (**ZnBDP_NO$_2$**) to 30 m^2 g^{-1} (**ZnBDP_NO$_2$@RAPTA-C**); from 1420 m^2 g^{-1} (**ZnBDP_NH$_2$**) to 140 m^2 g^{-1} (**ZnBDP_NH$_2$@RAPTA-C**) and 60 m^2 g^{-1} (**ZnBDP_NH$_2$@Mitoxantrone**); and from 1020 m^2 g^{-1} (**ZnBDP_OH**) to 215 m^2 g^{-1} (**ZnBDP_OH@RAPTA-C**) (Figure S19 and Table 3). In addition, the presence of the main bands characteristic of the pure drug (RAPTA-C or mitoxantrone) within the IR spectra of the loaded matrices is also in agreement with the incorporation of the drug (Figures S24).

For a further understanding of the drug adsorption process, we studied in detail the solid-liquid adsorption isotherm of RAPTA-C into the **ZnBDP_H** matrix at 25 ºC. The results show a type I adsorption isotherm (Figure 4), whose data can be satisfactorily fitted to the linear form of the Langmuir model (eq. (2)):

$$C/n = C/n_m + 1/(Kn_m) \qquad (2)$$

where C is the concentration of RAPTA-C in the methanolic solution (M) at the equilibrium, n is the amount of RAPTA-C incorporated in **ZnBDP_H** (mmol g^{-1}), K is the Langmuir equilibrium constant and n_m corresponds to the predicted saturation loading of RAPTA-C in **ZnBDP_H** (mmol g^{-1}). The results show a maximum loading n_m value of 2.07 mmol (0.959 g) of RAPTA-C *per* gram of **ZnBDP_H**. It should be highlighted that this high loading value corresponds to 0.55 mmol of RAPTA-C *per* mmol of **ZnBDP_H**, and confirms the results obtained by elemental analysis, UV-vis and attenuated total reflectance (ATR).

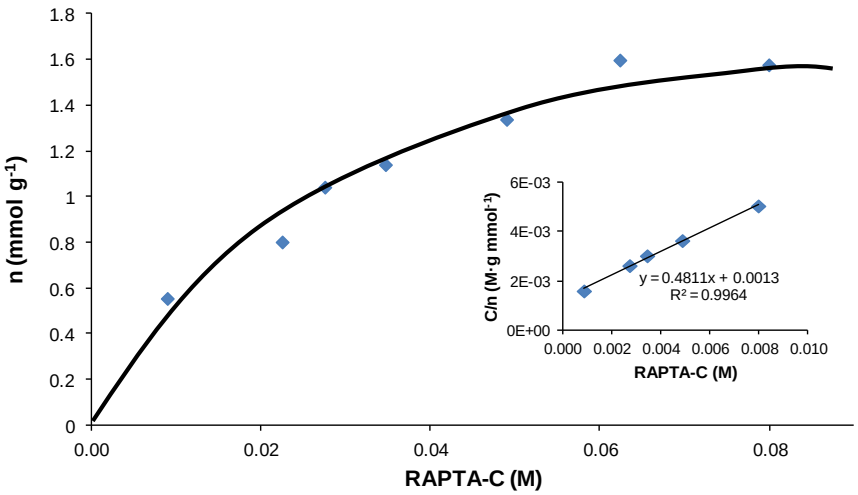

Figure 4. Solid-liquid adsorption isotherm of RAPTA-C into the **ZnBDP_H** matrix at 25 ºC. The inset shows the linear fitting of the data to the Langmuir model.

Finally, the RAPTA-C delivery from the **ZnBDP_X** series was studied in simulated body fluid (SBF) at 37 ºC under continuous stirring. The RAPTA-C kinetics of delivery was registered by measuring the delivered RAPTA-C in the supernatant solutions of SBF by means of UV-vis. At the same time, the possible H_2BDP_X leaching was followed in order to consider the matrix degradation upon drug release. Noteworthy, the drug delivery process, at a constant volume (150 mL) of SBF, is dependant of pore functionalization and exhibits two steps (less evident in **ZnBDP@RAPTA-C** and **ZnBDP_NO_2@RAPTA-C** systems) (Figure 5). The stepwise delivery might be related to framework flexibility and adaptability of the pore matrices. Indeed, this type of behaviour was already described for ibuprofen delivery from the highly flexible MIL-53 matrix.[79] Additionally, considering the rather good chemical stability of **ZnBDP_X** (X = H, NH_2 and NO_2) under the release conditions (after 48 h, only about 5% of the total ligand was delivered to the medium; Figure S21), the RAPTA-C release does not depend on the matrix degradation. In contrast, the drug release from **ZnBDP_OH@RAPTA-C** follows the same trend

than the matrix degradation (*ca.* 65% of BDP_OH ligand is leached after 48 h), suggesting an important effect of the chemical stability of the **ZnBDP_OH** solid over the RAPTA-C delivery.

It should be highlighted that the first and second steps of the desorption profiles (for **ZnBDP_NH$_2$** and **ZnBDP_OH**) can be satisfactory fitted to a first order kinetic model according to equation 3:

$$q_E - q_t = q_E e^{-kt} \qquad (3)$$

where q_E and q_t are the amounts of RAPTA-C released *per* gram of MOF (mmol g^{-1}) at the equilibrium and at the time t (h), respectively, and k is the first order kinetic constant (h^{-1}). The fitting of the data gives rise to different half-life times for the release of the metallodrug (Table 4), with the slower kinetics of release being observed for **ZnBDP_NH$_2$** and **ZnBDP_OH**. These results indicate that the polar matrix **ZnBDP_NH$_2$** might exhibit stronger interactions with RAPTA-C molecules than the less polar **ZnBDP_H** and **ZnBDP_NO$_2$** nanomaterials. In addition, **ZnBDP_NH$_2$** accounts for a lower pore volume than **ZnBDP_H** and **ZnBDP_NO$_2$** (0.677 *vs* 0.959 and 0.822 cm^3 g^{-1}, respectively) (Table 3), which may result in a slow-down of the RAPTA-C diffusion in the former case. Furthermore, in **ZnBDP_OH**, UV-vis studies of H_2BDP_X leaching (Figure S21) demonstrated that the drug release also depends on the kinetics of MOF degradation as RAPTA-C delivery from **ZnBDP_OH** is accompanied by a concomitant and progressive matrix degradation (up to 65%) due to the higher polarity of the BPD_OH ligand. In conclusion, the RAPTA-C release from the matrices might be affected by a combination of factors, such as: *i)* drug interaction with the matrix surface, *ii)* drug diffusion throughout the pores, controlled by the flexibility of the structures and pore volume, and *iii)* kinetics of degradation of the **ZnBDP_X** matrices.

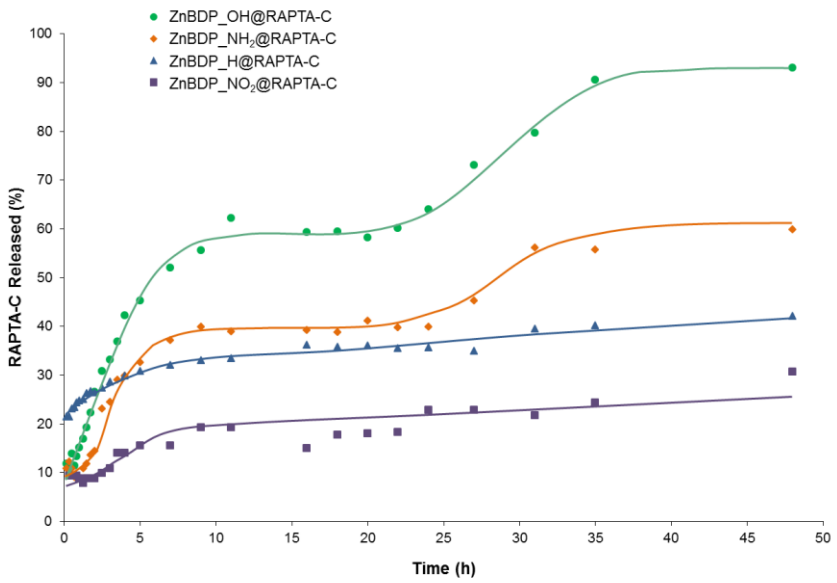

Figure 5. RAPTA-C release from **ZnBDP_X@RAPTA-C** (X = H, NH_2, NO_2 and OH) (10 mg) into a simulated body fluid (150 mL) at 37 ºC (top). For the sake of clarity, error bars have been removed from the plots (available in the Supporting Information, Figure S22). Note that lines are only visual guides.

Table 4. *K* values (h^{-1}) and $t_{1/2}$ obtained in the delivery of RAPTA-C from the series **ZnBDP_X** (X = H, NH_2, NO_2 and OH)

	ZnBDP_H	**ZnBDP_NH$_2$***		**ZnBDP_NO$_2$**	**ZnBDP_OH***	
		1st	*2nd*		*1st*	*2nd*
K (h^{-1})	0.5221	0.2878	0.1472	0.6074	0.2623	0.1109
$t_{1/2}$ (h)	1.33	2.08	4.71	1.14	2.64	6.25

* *K* and $t_{1/2}$ values were calculated, on the 1st and 2nd step of the RAPTA-C desorption data.

Furthermore, we have also studied the encapsulation of mitoxantrone into the **ZnBDP_X** porous matrices (X = H and NH_2) using an alternative solid state procedure, by grounding together a mixture of the corresponding MOF and mitoxantrone. Then, the mixture was washed

with acetone in order to eliminate the non-adsorbed mitoxantrone and the loaded **ZnBDP_X@Mitoxantrone** systems were recovered. This non conventional method allows the rapid incorporation, in only 20 minutes, of the drug into the porous matrices. Noteworthy, diffuse reflectance (DR) spectrum of **ZnBDP_X@Mitoxantrone** system is consistent with a significant narrowing of the broad band centred at 600 nm found in mitoxantrone in the solid state (Figure 6). This result should be related to the loss of the stacking interactions of the anthracene residues as a consequence of mitoxantrone confinement into the 1D pores of 1 nm diameter (Figure 6). Noteworthy, the shape of the electronic spectra of the hosted mitoxantrone molecules is similar to the one found in diluted aqueous solutions, in which there is no stacking interactions.[81] Thus, it can be concluded that the adsorption of mitoxantrone molecules into the 1D MOF's pores involves the loss of π-π stacking interactions.[82,83]

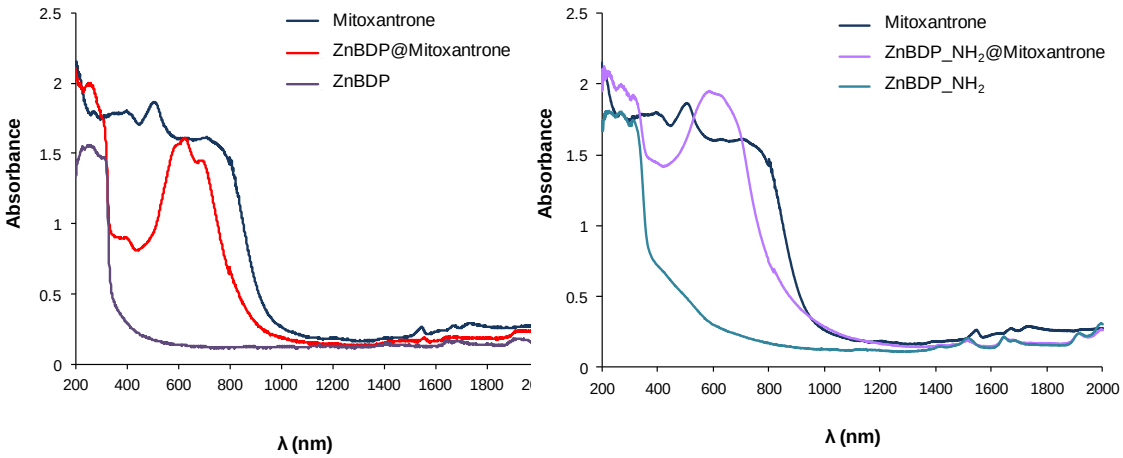

Figure 6. Diffuse reflectance spectrum of **ZnBDP_H**, **ZnBDP_H@Mitoxantrone**, **ZnBDP_NH₂**, **ZnBDP_NH₂@Mitoxantrone** and mitoxantrone.

Regarding mitoxantrone delivery in SBF (pH ~ 7.4) from the loaded **ZnBDP_X@Mitoxantrone** matrices, it should be pointed that the tendency of mitoxantrone to

precipitate at pH 6 to 8[84] which hampers here any accurate determination of the delivery process in this medium. Further investigations are being made in order to study the complex delivery of mitoxantrone from the **ZnBDP_X** matrices. The latter result should be taken as a proof of concept of the potential use of metal-organic frameworks as carriers of anticancer drugs.

4. CONCLUSIONS

We have successfully prepared small and monodispersed nanoparticles (~ 100 to 200 nm) of the isoreticular Zn bis-pyrazolate MOFs **ZnBDP_X** (H_2BDP = 1,4-bis(1H-pyrazol-4-yl)-2-X-benzene, X = H, NO_2, NH_2, OH) by optimizing the synthetic conditions, even using biofriendly conditions. The aqueous colloidal stability of these systems strongly depends on the pH and on the functional group, as a consequence of the differences in terms of outer surface species. Moreover, as a model case, the chemical, structural and colloidal stability of **ZnBDP_OH** was investigated under different relevant biological conditions simulating intravenous (albumin-PBS solutions) and oral (SIF complemented with pancreatin or mucin) administration routes, demonstrating a good structural and colloidal stability. This result may be attributed to the formation of a protein (albumin or pancreatin for intravenous or oral conditions, respectively) corona on their surface that prevents from **ZnBDP_OH** nanoparticles aggregation. On the other hand, the rapid aggregation of **ZnBDP_OH** in SIF supplemented with mucin indicates that these nanoparticles are able to interact with mucin suggesting a potential oral bioadhesion, usually associated with longer intestinal residence times.

Finally, the encapsulation and release of the antitumor drugs mitoxantrone and RAPTA-C were evaluated in the **ZnBDP_X** series as a proof of concept of the effect of the framework functionalization in the incorporation/delivery of these bioactive molecules. Firstly, it should be

noted that important loadings of both mitoxantrone and RAPTA-C drugs (up to 0.50 and 0.55 $mmol.mmol^{-1}$, respectively) were achieved by using a simple and fast impregnation method. In addition, the incorporation of mitoxantrone can also be achieved by simple grinding. Drug loading depends on the functional group of **ZnBDP_X** series, following the trend of the BET surface area of the functionalized solids. On the other hand, the RAPTA-C delivery in simulated body fluid takes place in two different steps, which could be related to the framework flexibility. In addition, while drug release from **ZnBDP_X** (X = H, NH_2 and NO_2) is independent on the matrix stability, the RAPTA-C delivery strongly depends on the kinetics of framework degradation in **ZnBDP_OH@RAPTA-C**. Indeed, among the highly stable matrixes, the polar **ZnBDP_NH_2** shows a slower rate of delivery, probably associated with stronger drug-matrix interactions and hindered diffusion, compared with **ZnBDP_NO_2** and **ZnBDP_H** analogues. These results highlight the effect of the functionalization of the MOF cavities on the chemical and colloidal stability as well as on the drug encapsulation and release kinetics.

ASSOCIATED CONTENT

Supporting Information. XRPD and FEG-SEM images of **ZnBDP_X** nanoparticles; XRPD stability tests and size and ζ-potential evolution measurements of **ZnBDP_OH** in the different simulated physiological media; ATR, IR spectra, XRPD patterns and TGA of **ZnBDP_X** and **ZnBDP_X@drug**. "This material is available free of charge via the Internet at http://pubs.acs.org."

AUTHOR INFORMATION

Corresponding Author

*Department of Inorganic Chemistry, University of Granada. Av. Fuentenueva S/N, 18071 Granada, Spain, ebaream@ugr.es; Institut Lavoisier, CNRS UMR8180, Université de Versailles St-Quentin en Yvelines, 45 Avenue des Etats-Unis, 78035 Versailles Cedex, France; patricia.horcajada@uvsq.fr

ACKNOWLEDGMENT

The Spanish Ministry of Economy and Competitivity (projects CTQ2011-22787/PPQ and CTQ2014-53486R), Junta de Andalucía (project P09-FQM-4981 and SR predoctoral grant) and COST action CM1105 are gratefully acknowledged for generous funding. PH and CS acknowledge CNRS, Université of Versailles St Quentin and the Labex Nanosaclay (reference ANR-10-LABX-0035) for the financial support.

REFERENCES

[1] Kroll, A.; Pillukat, M. H.; Hahn, D.; Schnekenburger, J. *Eur. J. Pharm. Biopharm.* **2009**, *72*, 370–377.

[2] Thomas, D. G.; Pappu, R. V.; Baker, N. A. *J. Biomed. Inform.* **2011**, *44*, 59–74.

[3] Torchilin, V. P. *Nanoparticulates as drug carriers*. Imperial College Press Ed., **2006**.

[4] Quartapelle-Procopio, E.; Rojas, S.; Padial, N.; Galli, S.; Masciocchi, N.; Linares, F.; Miguel, D.; Oltra, J. E.; Navarro, J. A. R.; Barea, E. *Chem. Commun.* **2011**, *47*, 11751–11753.

[5] Rojas, S.; Quartapelle-Procopio, E.; Wheatley, P. S.; Gil, B.; Marszalek, B.; Morris, R. E.; Barea, E. *CrystEngComm* **2013**, *15*, 9364–9367.

[6] Rojas, S.; Quartapelle-Procopio, E.; Carmona, F. J.; Romero, M. A.; Navarro, J. A. R.; Barea, E. *J. Mater. Chem. B* **2014**, *2*, 2473–2477.

[7] Rocca, J. D.; Liu, D.; Lin, W. *Acc. Chem. Res.* **2011**, *44*, 957–968.

[8] Horcajada, P.; Gref, R.; Baati, T.; Allan, P. K.; Maurin, G.; Couvreur, P.; Férey, G.; Morris, R. E.; Serre, C. *Chem. Rev*. **2012**, *112*, 1232–1268.

[9] Meyers, S. R.; Grinstaff, M. W. *Chem. Rev.* **2012**, *112*, 1615–1632.

[10] Nel, A. E.; Mädler, L.; Velegol, D.; Xia, T.; Hoek, E. M. V.; Somasundaran, P.; Klaessig, F.; Castranova, V.; Thompson, M. *Nat. Mater*. **2009**, *8*, 543–557.

[11] Moddaresi, M.; Brown, M. B.; Zhao, Y.; Tamburic, S.; Jones, S. A. *Intern. J. Pharmac*. **2010**, *400*, 176–182.

[12] Tamames-Tabar, C.; Cunha, D.; Imbuluzqueta, E.; Ragon, F.; Serre, C.; Blanco-Prieto, M. J.; Horcajada, P. *J. Mater. Chem. B* **2014**, *2*, 262–271.

[13] Gref, R.; Agostoni, V.; Daoud-Mahammed, S.; Rodriguez-Ruiz, V.; Malanga, M.; Jicsinszki, L.; Horcajada, P.; Serre, C. WO 2013178954 A1, **2013**.

[14] Carné-Sánchez, A.; Bonnet, C. S.; Imaz, I.; Lorenzo, J.; Tóth, É.; Maspoch, D. *J. Am. Chem. Soc.* **2013**, *135*, 17711–17714.

[15] Bellido, E.; Guillevic, M.; Hidalgo, T.; Santander-Ortega, M.; Serre, C.; Horcajada, P. *Langmuir* **2014**, *30*, 5911–5920.

[16] Aguilera-Sigalat, J.; Fox-Charles, A.; Bradshaw, D. **2014**, *50*, 4711–4713.

[17] Au, K. M.; Satterlee, A.; Min, Y.; Tian, X.; Kim, Y. S.; Caster, J. M.; Zhang, L.; Zhang, T.; Huang, L.; Wang, A. Z. *Biomaterials*. **2016**, *82*, 178-193.

[18] Wuttke, S.; Braig, S.; Preiß, T.; Zimpel, A.; Sicklinger, J.; Bellomo, C.; Rädler, J. O.; Vollmar A. M.; Bein, T. *Chem. Commun.* **2015**, *51*, 15752-15755.

[19] Farrusseng, D. *Metal-Organic Frameworks. Applications from Catalysis to Gas Storage*. Willey-VCH, **2011**.

[20] Ensign, L. M.; Cone, R.; Hanes, J. *Adv. Drug Deliv. Rev.* **2012**, *63*, 557–570.

[21] Chalati, T.; Horcajada, P.; Couvreur, P.; Serre, C.; Maurin, G.; Gref, R. *Nanomedicine.* **2011**, *6*, 1657-1660.

[22] Low, J. J.; Benin, A. I.; Jakubczak, P.; Abrahamian, J. F.; Faheem, S. A.; Willis, R. R. *J. Am. Chem. Soc.* **2009**, *131* (43), 15834-15842.

[23] Zhang, J. -P.; Zhang, Y. -B.; Lin, J. -B.; Chen, X. -M. *Chem Rev*. **2012**, *112*, 1001-1033.

[24] Colombo, V.; Galli, S.; Choi, H. J.; Han, G. D.; Maspero, A.; Palmisano, G.; Masciocchi, N.; Long, J. R. *Chem. Sci.* **2011**, *2*, 1311-1319.

[25] Colombo, V.; Montoro, C.; Maspero, A.; Palmisano, G.; Masciocchi, N.; Galli, S.; Barea, E.; Navarro, J. A. R. *J. Am. Chem. Soc*. **2012**, *134*, 12830–12843.

[26] Galli, S.; Masciocchi, N.; Colombo, V.; Maspero, A.; Palmisano, G.; López-Garzón, F. J.; Domingo-García, M.; Fernández-Morales, I.; Navarro, J. A. R. *Chem. Mater*. **2010**, *22*, 1664–1672.

[27] Mishra, D.; Hubenak, J. R.; Mathur, A. B. *J. Biomed. Mater. Res-A.* **2013**, *101A*, 12, 3646-3660.

[28] Daughton, C. G.; Ternes, T. A. *Environ. Health Persp.* **1999**, *107*, 907-938.

[29] Lippert, B. *Cisplatin, Chemistry and Biochemistry of a Leading Anti-Cancer Drug*, ed., Wiley-VCH, Weinheim, **1999**.

[30] Fricker S. P. *Dalton Trans.* **2007**, 4903–4917.

[31] Casini, A.; Edafe, F.; Erlandsson, M.; Gonsalvi, L.; Ciancetta, A.; Re, N.; Ienco, A.; Messori, L.; Peruzzini, M.; Dyson, P. J. *Dalton Trans.* **2010**, *39*, 5556–5563.

[32] Amouri, H.; Moussa, J.; Renfrew, A. K.; Dyson, P. J.; Rager, M. N.; Chamoreau, L.-M. *Angew. Chem., Int. Ed.* **2010**, *49*, 7530–7695.

[33] Yan, Y. K.; Melchart, M.; Habtemarian, A.; Peacock, A. F. A.; Sadler, P. J. *J. Biol. Inorg. Chem.* **2006**, *11*, 483–488.

[34] Scolaro, C.; Bergamo, A.; Brescacin, L.; Delfino, R.; Cocchietto, M.; Laurenczy, G.; Geldbach, T. J.; Sava, G.; Dyson, P. J. *J. Med. Chem.* **2005**, *48*, 4161– 4171.

[35] Xia, C.; Guoli, S.; Jianhui, J.; Roquin, Y. *Anal. Lett.* **1999**, *32*, 717–727.

[36] Chen, K. X.; Gresh, N.; Pullman, B. *Nucleic Acid Res.* **1986**, *14*, 3799–3812.

[37] Cornbleet, M. A.; Stuart-Harris, R. C.; Smith, I. E.; Coleman, R. E.; Rubens, R. D.; McDonald, M.; Mouridsen, H. T.; Rainer, H.; Van Oosteram, A. T.; Smyth, J. F. *Eur. J. Cancer Clin. Oncol.* **1984**, *20*, 1141–1146.

[38] Feofanov, A.; Sharonov, S.; Fleury, F.; Kudelina, I.; Nabiev, I. *Biophysics J.* **1997**, *73*, 3328–3336.

[39] Maspero, A.; Galli, S.; Masciocchi, N.; Palmisano, G. *Chem. Letters*, **2008**, *37*, 956-957.

[40] Allardyce, C. S.; Dyson, P. J.; Ellis, D. J.; Heath, S. *Chem. Commun*. **2001**, 1396–1397.

[41] Klug, P.; Alexander, L. E. *X-Ray diffraction procedures for polycrystalline and amorphous materials*. Wiley-VCH Ed. **1974**.

[42] Abramoff, M. D.; Magelhaes, P. J.; Ram, S. J. *Biophotonics Int*. **2004**, *11*, 36–43.

[43] *European Pharmacopeia 7.0*, **2010**.

[44] Kokubo, T.; Kushitani, H.; Ohtsuki, C.; Sakka, S.; Yamamuro, T. *J. Mater. Sci.: Mater. Med.* **1992**, *3*, 79–83.

[45] Scolaro, C.; Hartinger, C. G.; Allardyce, C. S.; Keppler, B. K.; Dyson, P. J. *J. Inorg. Biochem.* **2008**, *102*, 1743–1748.

[46] Flügel, E. A.; Ranft, A.; Haase, F.; Lotsch, B. V. *J. Mater. Chem.* **2012**, *22*, 10119–10113.

[47] Ranft, A.; Betzler, S. B.; Haase, F.; Lotsch, B. V. *Cryst. Eng. Comm.* **2013**, *15*, 9296–9300.

[48] Goldberg, M.; Langer, R.; Jia, X. *J. Biomat. Sci*. **2007**, *18*, 241–68.

[49] Elsabahy, M.; Wooley, K. K. *Chem. Soc. Rev*. **2012**, *41*, 2545–2561.

[50] Pourbaix, M. *Atlas of Electrochemical Equilibria in Aqueous Solutions*. National Association of Corrosion Engineers, **1974**.

[51] Sun, C. –Y.; Qin, C.; Wang, X. –L.; Yang, G. –S.; Shao, K. –Z.; Lan, Y. –Q.; Su, Z. –M.; Huang, P.; Wang, C. –G.; Wang E. –B. *Dalton Trans.* **2012**, *41*, 6906–6909.

[52] Pourbaix diagrams of zinc were calculated for $[Zn^{2+}] = 10^{-4}$ M at 25 ºC using the Hydra and Medusa software.

[53] Weatherby, D.; Fergusson, S. *Blood Chemistry and CBC Analysis, Quick reference guide*. Vis Medicatrix Press, **2004**.

[54] Santander-Ortega, M. J.; de la Fuente, M.; Lozano, M. V.; Tsui, M. L.; Bolton, K.; Uchegbu, I. F.; Schätzlein, A. G. *Curr. Top. Med. Chem*. **2014**, *14*, 1172–81.

[55] Santander-Ortega, M. J.; Uchegbu, I. F.; Schätzlein, A. G. *Dendrimer-Based Gene Delivery Systems: Administration Routes and In Vivo Evaluation in Dendrimer-Based Drug Delivery Syestems: from Theory to Practice*, Wiley&Sons Ed. **2012**, *9*, 329–354.

[56] Hiemenz, P. C.; Rajogopalan, R. *Principles of Colloidal and Surface Chemistry*, Dekker Ed., **1997**.

[57] Peula, J. M.; de las Nieves, F. J. *Colloids Surf. A: Physicochem. Eng. Aspects*, **1994**, *90*, 55–62.

[58] Casals, E.; Pfaller, T.; Duschl, A.; Janneke Oostingh, G.; Puntes, V. *ACS Nano*, **2010**, *4*, 3623–3632.

[59] Cedervall, T.; Lynch, I.; Foy, M.; Berggård, T.; Donnelly, S. C.; Cagney, G.; Linse, S.; Dawson, K. A. *Angew. Chem. Int. Ed*. **2007**, *46*, 5754–5756.

[60] Wright, A. K.; Thompson, M. R. *Biophys. J*. **1975**, *15*, 137–141.

[61] Lai, S. K.; Wang, Y.; Wirtz, D.; Hanes, J. *Adv. Drug Deliv. Rev.* **2009**, *61*, 86–100.

[62] Jin, F.; Li, J.; Ye, X.; Wu, C. *J. Phys. Chem. B*. **2007**, *111*, 11745–11749.

[63] Jodar-Reyes, A. B.; Martin-Rodriguez, A.; Ortega-Vinuesa, J. L. *J. Coll. Interface Sci*. **2006**, *298*, 248–257.

[64] Kenmogne-Domguia, H.; Meynier, A.; Viau, M.; Llamas, G.; Genot, C. *Food Funct.* **2012**, *3*, 1302–1309.

[65] Kufe, D. W. *Nat. Rev. Cancer*. **2009**, *9*, 874– 885.

[66] Harding, S.; Davis, S.; Deacon, M.; Fiebrig, I. *Biotechnol. Genet. Eng. Rev.* **1999**, *16*, 41–86.

[67] Smart, J. D. *Adv. Drug Deliv. Rev.* **2005**, *57*, 1556–1568.

[68] https://www.nrv.gov.au/nutrients/zinc (accessed in 2015)

[69] Plum, L. M.; Rinck, L.; Haase, H. *Int. J. Environ. Res. Public Health*, **2010**, *7*, 1342-1365

[70] Horcajada, P.; Chalati, T.; Serre, C.; Gillet, B.; Sebrie, C.; Baati, T.; Eubank, J. F.; Heurtaux, D.; Clayette, P.; Kreuz, C.; Chang, J.-S.; Hwang, Y. K.; Marsaud, V.; Bories, P.-N.; Cynober, L.; Gil, S.; Férey, G.; Couvreur P.; Gref, R. *Nat. Mater*, **2010**, *9*, 172-178.

[71] Imaz, I.; Rubio-Martinez, M.; An, J.; Sole-Font, I.; Rosi, N. L.; Maspoch, D. *Chem. Commun*. **2011**, *47*, 7287-7302.

[72] Kura, A. U.; Hussein, M. Z.; Fakurazi, S.; Arulselvan, P. *Chem. Cent. J.* **2014**, *8*, 47, 1-8.

[73] Ghaderi, S.; Ramesh, B.; Seifallian, A. M. *J. Drug Target.* **2011**, *19* (7), 475–486.

[74] Dwivedi, P.; Khatik, R.; Khandelwal, K.; Srivastava, R.; Taneja, I.; Rama Raju, K. S.; Dwivedi, H.; Shukla, P.; Gupta, P.; Singh, S.; Tripathi, R.; Paliwal, S. K.; Wahajuddin Dwivedi, A. K.; Mishra, P. R. *RSC Adv.* **2014**, *4*, 64905–64918.

[75] Gómez-Canela, C.; Campos, B.; Barata, C.; Lacorte, S. *Int. J. Environ. Sci. Technol*. **2015**, *12*, 633–640.

[76] Rantanen, V.; Grénman, S.; Kulmala, J.; Grénman, R. *Brit. J. Cancer*, **1994**, *69*(3), 482–486.

[77] Llewellyn, P. L.; Bourrelly, S.; Serre, C.; Filinchuk, Y.; Férey, F. *Angew. Chem., Int. Ed.* **2006**, *45*, 7751–7754.

[78] Choi, H. J.; Dinca, M.; Long, J. R. *J. Am. Chem. Soc*. **2008**, *130*, 7848–7850.

[79] Horcajada, P.; Serre, C.; Maurin, G.; Ramsahye, N. A.; Balas, F.; Vallet-Regí, M.; Sebban, M.; Taulelle, F.; Férey, G. *J. Am. Chem. Soc.* **2008**, *130*, 6774–6780.

[80] Gregg, S. J.; Sing, K. S. W. *Adsorption, Surface Area and Porosity*. Academic Press INC (London), **1982**.

[81] Enache, M.; Volanschi, E. *J. Pharm. Pharmacol*. **2012**, *64*, 688-696.

[82] Sonoda, Y. *Molecules* **2011**, *16*, 119–148.

[83] Inayama, S.; Tatewaki, Y.; Okada, S. *Polym. J*. **2010**, *42*, 201–207.

[84] Heister, E.; Neves, V.; Lamprecht, C.; Silva, S. R. P.; Coley, H. M.; McFadden, J. *Carbon*, **2012**, *50*, 622–632.

FOR TABLE OF CONTENT ONLY

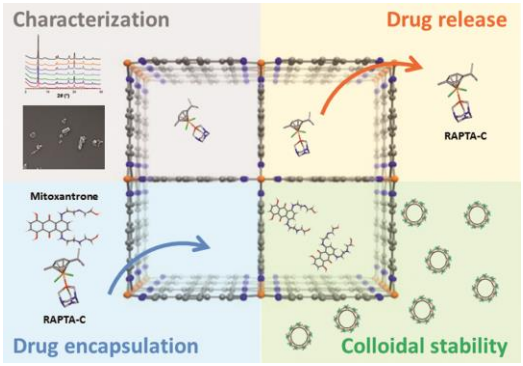

Isoreticular Zn-bispyrazolate MOF nanoparticles exhibit a good structural and colloidal stability in simulated physiological media (intravenous conditions) probably due to the formation of a protein corona on their surface that prevents their aggregation. Furthermore, these materials have been tested for the encapsulation and delivery of two antitumor drugs (mitroxantrone and [Ru(p-cymene)Cl_2(pta)]; pta = 1,3,5-triaza-7-phospaadamantane, RAPTA-C). The results show that ligand functionalization significantly affects both the delivery kinetics and the total amount of released drug.